MARS SCIENCE LABORATORY ENTRY, DESCENT AND LANDING TRAJECTORY RECONSTRUCTION UNCERTAINTY ASSESSMENT

Prasad Kutty[(1)], Christopher Karlgaard[(2)]

[(1)] Student – Georgia Institute of Technology, Analytical Mechanics Associates, Inc., M.S. 489, NASA Langley Research Center, Hampton, VA 23681, Email:prasad.kutty@nasa.gov
[(2)]Analytical Mechanics Associates, Inc., M.S. 489 NASA Langley Research Center, Hampton, VA 23681, Email:chris.karlgaard-1@nasa.gov

ABSTRACT

On August 5th, 2012 the Mars Science Laboratory (MSL) entry vehicle successfully entered and landed on the Mars surface. During Entry Descent and Landing (EDL), the Curiosity rover was carried by the entry vehicle and carefully lowered to the ground near Gale crater. After completion of the EDL mission, trajectory reconstruction analyses were performed in order to assess the performance of the entry vehicle and compare its performance against pre-flight predictions. Three semi-independent methods of reconstruction were performed, each relying on unique input data sets. Uncertainty estimates of the outputs computed by each reconstruction were also generated. The uncertainty analysis for one of the reconstruction methods, the aerodatabase reconstruction method, is a novel approach not seen in previous literature. This paper discusses the three reconstruction techniques and details the algorithms used to evaluate their uncertainties.

1. INTRODUCTION

The Mars Science Laboratory (MSL) entry vehicle successfully entered the Mars atmosphere and delivered the Curiosity rover to the Mars surface on August 5th, 2012. In addition to safely landing the rover, the entry vehicle returned valuable Entry Descent and Landing (EDL) data to earth for a variety of purposes, including trajectory reconstruction. Three semi-independent reconstruction methods were utilized for the MSL EDL – an inertial reconstruction, an aerodatabase reconstruction, and a Mars Entry Atmospheric Data System (MEADS) based reconstruction. Each method relied on distinct measurements taken by the MSL entry vehicle during EDL to compute time histories of common trajectory parameters, such as position, velocity, attitude, dynamic pressure, angle of attack, and angle of sideslip. In addition to performing the reconstruction of the entry trajectory, an uncertainty assessment was performed in order to identify the accuracy of each analysis technique. The uncertainty or error assessment captures the statistical variances of the reconstructed outputs based on the known uncertainties of the measurements used to generate those reconstructions. This paper is concerned specifically with the uncertainty assessments of the three reconstruction analyses.

The inertial reconstruction was performed by integration of the non-linear dynamic equations of motion of the vehicle state. This deterministic approach relied only on the measured accelerations and angular rates from the inertial measurement unit (IMU), as well as the initial condition of the entry vehicle. Similarly, the input uncertainties and linear system dynamic matrices were used to integrate the covariance dynamic equations and determine the uncertainties associated with the inertial reconstruction outputs. This approach, sometimes called a deterministic or navigated solution, is a common reconstruction technique [1-6]. It was used to provide an initial uncertainty assessment as an input to other analysis methods.

The aerodatabase reconstruction was applied to extract angle of attack and angle of sideslip by solving a non-linear system of equations relating accelerations from the IMU to force coefficients from the MSL aerodynamic database. Additionally, estimates of density, pressure, and Mach number were recovered through computations involving the aerodatabase. Linear sensitivity matrices for each non-linear reconstruction equation were computed and a covariance mapping computation was performed to transform the input uncertainties into the reconstructed output uncertainties. The input uncertainties were known beforehand, either through measurement specifications or previous analysis, such as the inertial reconstruction. While this method of reconstruction has been previously used on several planetary missions (such as Pathfinder [2-3], Mars Exploration Rover [5], and Phoenix [6]), the covariance mapping technique to determine output uncertainties is a technique not previously applied to the problem and is a new result given in this paper.

The MEADS-based pressure reconstruction makes use of seven forebody pressure measurements as a Flush Air Data System (FADS) to produce estimates of the angle of attack, angle of sideslip, dynamic pressure, static pressure, and Mach number. The estimates are obtained from a nonlinear weighted least-squares algorithm at each measurement time. A novel IMU-aiding approach has been implemented in which the IMU velocity estimate is combined with MEADS-derived speed of sound to produce an initial estimate of the Mach number. This initial estimate is then refined in the nonlinear weighted least-squares algorithm. The algorithm is iterated globally over the entire data set until the estimated speed of sound profile (and, consequently, Mach number) converges. The uncertainties in the computed quantities arise naturally as a byproduct of the weighted least-squares algorithm, corresponding to the covariance matrix of the converged solution.

This paper provides an overview of the reconstruction algorithms and the mathematical details of the uncertainty analysis procedures and results of the MSL EDL reconstruction.

2. INERTIAL RECONSTRUCTION

The inertial reconstruction was performed using an IMU-based algorithm to integrate the equations of motion that define the entry vehicle's position, velocity and attitude. Sensed axial acceleration and angular rate measurements, obtained at a rate of 200Hz, were passed to the reconstruction algorithm, acting as a forcing function during integration. The initial condition of position, velocity and attitude were obtained from an orbit determination solution and star tracker update provided to the navigation filter prior to cruise stage separation. The equations of motion, which are detailed in [7], were integrated using a 4th order Runge Kutta numerical integrator at a rate of 200Hz.

The accuracy, or uncertainty, of the inertial reconstruction was estimated through propagation of the statistics of the state variables. Specifically, variances of the reconstructed states were computed through integration of the linear covariance dynamic equation, given in Eq. 1,

$$\dot{P} = AP + PA^T + BQB^T \tag{1}$$

where A is the matrix of partial derivatives of the system dynamics with respect to the state, P is the covariance of the state variables, B is the matrix of partial derivatives of the system dynamics with respect to the process noise, and Q is the process noise matrix.

In addition to the state parameters reconstructed through integration (position, velocity and attitude), several parameters, such as angle of attack and angle of sideslip, were computed through output transformations. Output transformations requiring atmospheric states (i.e. dynamic pressure) utilized an atmosphere model developed from preflight mesoscale models superimposed on the reconstructed trajectory. Uncertainties of the derived outputs were generated by transformation of the state covariance computed from Eq. 1 using a central difference transform [8]. The inertial uncertainty estimation was validated against Monte Carlo results from pre-flight simulations to offer confidence in the uncertainty predictions.

3. AERODATABASE RECONSTRUCTION

The aerodatabase reconstruction was used to obtain estimates of angle of attack, angle of sideslip, density, pressure, Mach number, temperature and dynamic pressure. Two loops were used to reconstruct these parameters – an outer loop performed reconstruction of the air data states and an inner loop performed reconstruction of angle of attack and sideslip. The outer loop begins by computing density from axial force coefficient obtained from the MSL aerodatabase. The equation for density is given in Eq. 2,

$$\rho = -\frac{2ma_x}{V^2 SC_A} \tag{2}$$

where m is the vehicle mass, a_x is the x-axis acceleration in the body frame, V is the vehicle velocity, S is the reference area of the vehicle and C_A is the axial force coefficient extracted from the aerodatabase. Note that the velocity of the vehicle used to compute density was obtained from the inertial reconstruction. Static pressure is computed next through an Euler integration of the hydrostatic equation. This computation is shown in Eq. 3,

$$p_k = p_{k-1} - \rho_k g_k \left(r_k - r_{k-1}\right) \tag{3}$$

where p_k is pressure at the current time, p_{k-1} is pressure at the previous time, ρ_k is the density at the current time, g_k is the current estimate of gravity based on altitude, r_k is the altitude at the current time and r_{k-1} is the altitude at the previous time. The estimate of pressure at the initial time was obtained from the inertial reconstruction. Mach number was computed next as given by Eq. 4,

$$M = V/c \tag{4}$$

where V is the vehicle velocity and c is the speed of sound. Finally, dynamic pressure was computed as given by Eq. 5,

$$\bar{q} = \frac{1}{2}\rho V^2 \tag{5}$$

where density was computed in Eq. 2 and velocity was obtained through the inertial reconstruction. After the air data states are computed using Eqs. 2-5, the inner loop is initiated to determine angle of attack and angle of sideslip.

The inner loop applied a Newton root solving algorithm to a non-linear system of equations that are functions of angle of attack and sideslip. The equations were derived from the ratios of axial force coefficient to normal and side force coefficient, yielding a relationship between the ratios of accelerations and force coefficients [9-10]. Rearranging the equations, as shown in Eq. 6, yields the non-linear system of equations to which the root finding algorithm was applied. The algorithm converges to values of angle of attack and sideslip for which the equations equal zero, corresponding to the angle of attack and sideslip at the current time.

$$f(\alpha,\beta) = \begin{Bmatrix} f_1(\alpha,\beta) \\ f_2(\alpha,\beta) \end{Bmatrix} = \begin{Bmatrix} \frac{a_z}{a_x} - \frac{C_N}{C_A} \\ \frac{a_y}{a_x} + \frac{C_Y}{C_A} \end{Bmatrix} = 0 \tag{6}$$

In Eq. 6, α is the angle of attack, β is the angle of sideslip, a_x, a_y and a_z are the body axis accelerations obtained from the IMU and transformed to the vehicle center of gravity, and C_A, C_Y and C_N are the axial, side, and normal force coefficients obtained from the aerodatabase. Plots of the IMU data during entry can be found in [11].

At each time point, the Newton solver algorithm is used to converge upon the roots of Eq. 6. Each iteration of the algorithm updates the independent variables of the function (angle of attack and sideslip) until the update between consecutive iterations is smaller than a chosen threshold. The update equation to the Newton solver is given by Eq. 7,

$$y_i = y_{i-1} - F(y_{i-1})^{-1} f(y_{i-1}) \tag{7}$$

where y_i is the updated value of the set of independent variables in Eq. 6 (angle of attack and sideslip), y_{i-1} is the value of the set of independent variables at the previous algorithm iteration, $F(y_{i-1})$ is the Jacobian matrix of partial derivatives of the function, f, with respect to independent variables at the previous iteration and $f(y_{i-1})$ is the function, f, evaluated at the previous iteration. Eq. 7 can be expanded in matrix form as shown by Eq. 8.

$$\begin{bmatrix} \alpha_i \\ \beta_i \end{bmatrix} = \begin{bmatrix} \alpha_{i-1} \\ \beta_{i-1} \end{bmatrix} - \begin{bmatrix} q & r \\ s & t \end{bmatrix} \begin{bmatrix} \left(a_{z,i-1}/a_{x,i-1}\right) - \left(C_{N,i-1}/C_{A,i-1}\right) \\ \left(a_{y,i-1}/a_{x,i-1}\right) + \left(C_{Y,i-1}/C_{A,i-1}\right) \end{bmatrix} \tag{8}$$

For convenience during the derivation of uncertainties, the inverse of the Jacobian has been substituted with a matrix whose elements are q, r, s and t. Also note that all of the terms on the right hand side of Eq. 8 are evaluated at the previous algorithm iteration. Once this algorithm converges upon updated values of angle of attack and sideslip, the updated values are passed to the outer loop of the reconstruction algorithm where the air data states are recomputed. The reconstruction at the current time is complete when the parameters estimated inside of each loop have converged.

3.1 Uncertainty estimation of air data states

The uncertainties associated with the reconstructed parameters were computed using a linear covariance transformation technique. The transformation maps input uncertainties to output uncertainties through linearization of the equations used to estimate the reconstructed states. This technique was performed for the uncertainty estimates of air data states as well as angle of attack and sideslip. The derivation of uncertainties for air data states is detailed in this section, and angle of attack and sideslip is given in the following section. Pre-flight evaluations of the uncertainties were performed through comparison with Monte Carlo results.

First, partial derivatives of each state estimate equation with respect to the equation's independent variables were taken, as shown in Eqs. 9-13 for the pressure estimate equation (Eq. 3).

$$\frac{\partial p_k}{\partial p_{k-1}} = 1 \tag{9}$$

$$\frac{\partial p_k}{\partial \rho_k} = -g_k\left(r_k - r_{k-1}\right) \tag{10}$$

$$\frac{\partial p_k}{\partial g_k} = -\rho_k\left(r_k - r_{k-1}\right) \tag{11}$$

$$\frac{\partial p_k}{\partial r_k} = -\rho_k g_k \tag{12}$$

$$\frac{\partial p_k}{\partial r_{k-1}} = \rho_k g_k \tag{13}$$

Using the partial derivatives computed in Eqs. 9-13, the variance in reconstructed pressure was determined by multiplying the vector of partial derivatives by the diagonal matrix of input variances, as shown in Eq. 14.

$$\sigma^2_{p_k} = \begin{bmatrix} \partial p_k / \partial p_{k-1} \\ \partial p_k / \partial \rho_k \\ \partial p_k / \partial g_k \\ \partial p_k / \partial r_k \\ \partial p_k / \partial r_{k-1} \end{bmatrix}^T \times \begin{bmatrix} \sigma^2_{p_{k-1}} & 0 & 0 & 0 & 0 \\ 0 & \sigma^2_{\rho_k} & 0 & 0 & 0 \\ 0 & 0 & \sigma^2_{g_k} & 0 & 0 \\ 0 & 0 & 0 & \sigma^2_{r_k} & 0 \\ 0 & 0 & 0 & 0 & \sigma^2_{r_{k-1}} \end{bmatrix} \times \begin{bmatrix} \partial p_k / \partial p_{k-1} \\ \partial p_k / \partial \rho_k \\ \partial p_k / \partial g_k \\ \partial p_k / \partial r_k \\ \partial p_k / \partial r_{k-1} \end{bmatrix} \tag{14}$$

The other air data state estimates (density, Mach number and dynamic pressure) were also computed using the linear covariance transformation approach. Although not shown in this paper, the partial derivatives of their state equations were taken and partial derivative terms similar to those in Eqs. 9-13 were obtained.

3.2 Uncertainty estimation of angle of attack and sideslip

Angle of attack and sideslip uncertainties were obtained using the same technique as the air data states, but taking the partial derivatives of Eq. 8 required numerical differentiation of the aerodynamic force coefficients. The derivation for the angle of attack uncertainty is detailed in the section below. While not shown in this paper, angle of sideslip uncertainty was derived in the exact same manner as angle of attack by replacing the angle of attack update equation with the angle of sideslip update equation. The derivation begins with the angle of attack update equation, extracted from the matrix form of Eq. 8 as shown in Eq. 15.

$$\alpha_i = \alpha_{i-1} - q\left(\frac{a_{z,i-1}}{a_{x,i-1}} - \frac{C_{N,i-1}}{C_{A,i-1}}\right) - r\left(\frac{a_{y,i-1}}{a_{x,i-1}} + \frac{C_{Y,i-1}}{C_{A,i-1}}\right) \tag{15}$$

First, the partial derivative of this equation was taken with respect to α_{i-1} as shown in Eq. 16. In Eq. 16, the partial derivatives of the ratios of force coefficients were evaluated using the quotient rule and the subsequent partial derivatives of the force coefficients were computed numerically using the aerodatabase.

$$\frac{\partial \alpha_i}{\partial \alpha_{i-1}} = 1 + q\frac{\partial}{\partial \alpha_{i-1}}\left(\frac{C_{N,i-1}}{C_{A,i-1}}\right) - r\frac{\partial}{\partial \alpha_{i-1}}\left(\frac{C_{Y,i-1}}{C_{A,i-1}}\right) \tag{16}$$

Eq. 15 was also differentiated with respect to velocity, Mach number and uncertainty factor because the force coefficients are functions of these parameters. This differentiation was performed by applying the chain rule, as shown in Eqs. 17-19. Note that the uncertainty factor is a set of constants provided to the aerodatabase as an input in order to apply multiplier and adder corrections to the force and moment coefficients to account for off-nominal behavior.

$$\frac{\partial \alpha_i}{\partial V_{i-1}} = \frac{\partial \alpha_i}{\partial C_{A,i-1}}\frac{\partial C_{A,i-1}}{\partial V_{i-1}} + \frac{\partial \alpha_i}{\partial C_{Y,i-1}}\frac{\partial C_{Y,i-1}}{\partial V_{i-1}} + \frac{\partial \alpha_i}{\partial C_{N,i-1}}\frac{\partial C_{N,i-1}}{\partial V_{i-1}} \tag{17}$$

$$\frac{\partial \alpha_i}{\partial M_{i-1}} = \frac{\partial \alpha_i}{\partial C_{A,i-1}}\frac{\partial C_{A,i-1}}{\partial M_{i-1}} + \frac{\partial \alpha_i}{\partial C_{Y,i-1}}\frac{\partial C_{Y,i-1}}{\partial M_{i-1}} + \frac{\partial \alpha_i}{\partial C_{N,i-1}}\frac{\partial C_{N,i-1}}{\partial M_{i-1}} \tag{18}$$

$$\frac{\partial \alpha_i}{\partial \vec{u}_{i-1}} = \frac{\partial \alpha_i}{\partial C_{A,i-1}}\frac{\partial C_{A,i-1}}{\partial \vec{u}_{i-1}} + \frac{\partial \alpha_i}{\partial C_{Y,i-1}}\frac{\partial C_{Y,i-1}}{\partial \vec{u}_{i-1}} + \frac{\partial \alpha_i}{\partial C_{N,i-1}}\frac{\partial C_{N,i-1}}{\partial \vec{u}_{i-1}} \tag{19}$$

In Eqs. 17-19, the differentiation of the force coefficients with respect to velocity, Mach number and uncertainty factor are performed numerically. The differentiation of angle of attack with respect to the force coefficients was computed analytically by differentiating Eq. 15 as shown in Eqs. 20-22.

$$\frac{\partial \alpha_i}{\partial C_{A,i-1}} = -q\frac{C_{N,i-1}}{C_{A,i-1}^2} + r\frac{C_{Y,i-1}}{C_{A,i-1}^2} \tag{20}$$

$$\frac{\partial \alpha_i}{\partial C_{Y,i-1}} = -\frac{r}{C_{A,i-1}} \tag{21}$$

$$\frac{\partial \alpha_i}{\partial C_{N,i-1}} = \frac{q}{C_{A,i-1}} \tag{22}$$

Finally, the output uncertainty transformation is performed by multiplying the vector of partial derivatives by the input covariance matrix. This is shown by Eq. 23.

$$\sigma_{\alpha_i}^2 = \begin{bmatrix} \partial\alpha_i/\partial\alpha_{i-1} \\ \partial\alpha_i/\partial V_{i-1} \\ \partial\alpha_i/\partial M_{i-1} \\ \partial\alpha_i/\partial \vec{u}_{i-1} \end{bmatrix}^T \times \begin{bmatrix} \sigma_{\alpha_{i-1}}^2 & 0 & 0 & 0 \\ 0 & \sigma_{V_{i-1}}^2 & 0 & 0 \\ 0 & 0 & \sigma_{M_{i-1}}^2 & 0 \\ 0 & 0 & 0 & \sigma_{\vec{u}_{i-1}}^2 \end{bmatrix} \times \begin{bmatrix} \partial\alpha_i/\partial\alpha_{i-1} \\ \partial\alpha_i/\partial V_{i-1} \\ \partial\alpha_i/\partial M_{i-1} \\ \partial\alpha_i/\partial \vec{u}_{i-1} \end{bmatrix} \tag{23}$$

4. MEADS PROCESSING ALGORITHM

4.1 Pressure Modeling and Model Uncertainty

A CFD (Computational Fluid Dynamics)-based table lookup model was developed for analysis of the MSL air data system. This CFD database is based on supersonic and hypersonic regime pressure distributions from thin—layer Navier-Stokes solutions generated using the Langley Aerothermal Upwind Relaxation Algorithm (LAURA). The CFD database is from the same set of solutions as the flight aerodynamic database that was utilized in the aerodatabase reconstruction. The CFD database pressures were nondimensionalized using the freestream pressure and dynamic pressure of each solution. The nondimensionalization transforms the forebody pressures into pressure coefficient, which allows the CFD solutions to be used across a wide range of trajectories with different density and velocity profiles.

Each CFD grid point consists of a full surface pressure distribution solution, with 37 clock angles in uniform 5 degree increments and 61 cone angles with non-uniform increments. These grid points can be interpolated as needed to provide estimates of the pressure distribution at any point on the aeroshell [11]. The pressures based on the CFD database are shown for a nominal trajectory in [11].

An uncertainty model of the CFD pressure distribution was developed to model various error sources, including basic wind tunnel to CFD differences, errors inherent to the wind tunnel data, deformation, OML (Outer Mold Line) change, grid refinement, ablation, protuberances, and port location uncertainties. Pressure measurement system error models consist of detailed transducer characterizations from thermal vacuum chamber calibrations, thermocouple measurement errors such that an inaccurate temperature is used in the calibration database, system noise and quantization, time tag errors and sampling delays, pressure path leaks, pneumatic lag, and thermal transpiration [12]. These error sources were combined to produce measurement uncertainty inputs required by the reconstruction algorithm.

4.2 MEADS Algorithm

The MEADS data processing algorithm is an IMU-aided pressure-based solution. In this approach, the IMU planet-relative velocity was used to aid the determination of Mach number in the solution for angle of attack, sideslip, dynamic pressure, and static pressure [12]. The IMU aiding approach avoids numerical issues associated with the weak observability of Mach number from pressures alone. The algorithm introduces Mach number as an additional pseudo-observation into a standard least-squares fit of the state variables to the measured pressures that otherwise resembles the algorithm used for the Shuttle Entry Air Data System (SEADS) [13]. In the MEADS processing algorithm, the modeled pressure distribution was based on CFD solutions, whereas the SEADS algorithm used a modified Newtonian flow model that was calibrated based on wind tunnel experiments. The MEADS algorithm is given as follows.

The atmospheric state vector was defined as $x = [\alpha, \beta, \bar{q}, p_s]$, where α is the angle of attack, β is the angle of sideslip, $\bar{q}$ is the dynamic pressure, and p_s is the static pressure. The quantity p is used to denote the vector of pressure measurements, and $h(x)$ is the CFD-based pressure model. Then, the measurement equation was written as

$$z = \tilde{h}(x) = \begin{Bmatrix} p \\ M \end{Bmatrix} = \begin{Bmatrix} h(x) \\ \sqrt{2\bar{q}/(\gamma p_s)} \end{Bmatrix} \tag{23}$$

The measurement model was approximated about a reference value, $\bar{x}$, using a first-order Taylor series expansion, given by Eq. 24.

$$z \approx \tilde{h}(\bar{x}) + \tilde{H}(x) \cdot (x - \bar{x}) \tag{24}$$

where $\tilde{H}$ is the Jacobian matrix of the measurement model evaluated at the reference condition. The preceding equation was recast as

$$\lambda = \tilde{H}(x)x \tag{25}$$

where $\lambda = z - \tilde{h}(\bar{x}) + \tilde{H}(\bar{x})\bar{x}$. This equation takes the form of a linear regression problem, which was solved using the weighted least-squares method to find the best fit to the data. The solution is given by Eq.26,

$$\hat{x} = \left(\tilde{H}^T R^{-1} \tilde{H}\right)^{-1} \tilde{H}^T R^{-1} \lambda \tag{26}$$

where R is the measurement covariance matrix.

Since the original relationship between the measurements and the states is nonlinear, the solution was iterated until convergence, by successively replacing x with $\hat{x}$. The covariance matrix of the state estimate error was computed using the relation in Eq.27.

$$\hat{P} = \left(\tilde{H}^T R^{-1} \tilde{H}\right)^{-1} \tag{27}$$

To apply the IMU aiding to the least-squares algorithm, an estimate of the speed of sound was needed to compute Mach number from the IMU-derived velocity. Since the algorithm computes a speed of sound estimate based on the computed density and static pressure, the algorithm was iterated globally by updating the speed of sound estimate on each pass, based on the derived speed of sound from the previous iteration. For the MEADS reconstruction, the initial speed of sound profile was assumed to be 220 m/s, constant with altitude. Additionally, systematic errors in the pressure model were estimated using a batch least-squares fit of a cubic polynomial error model to the measured residuals. Additional details on the MEADS processing algorithm can be found in [12].

4.3 Pre-Flight Uncertainty Analysis

Extensive pre-flight simulations were conducted to analyze the performance of the MEADS processing algorithm. These simulation studies included single variable sensitivity studies, linear covariance analysis, Monte Carlo analysis, and scale model flight testing at ballistic range facilities [14].

An example of the pre-flight uncertainty analysis is shown in Fig. 1. These results show the 3-σ uncertainties in the aerodynamic state estimate based on Monte Carlo statistics with a sample size of 2000 cases, and the predicted uncertainties based on the state covariance estimate computed within the MEADS least-squares processing algorithm. Note that the MEADS uncertainties were computed from a nominal simulation run around which the Monte Carlos were initialized. These results indicate that the predicted uncertainties based on the least-squares covariance matrix are a good match to the true statistics computed from the Monte Carlo simulation. This result gives confidence that the uncertainty predictions from the MEADS algorithm are accurate.

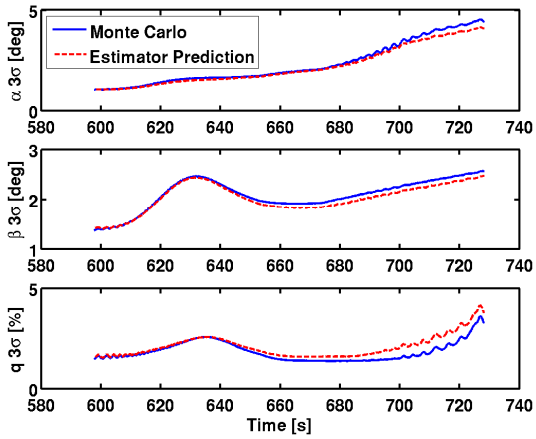

Fig 1. Pre-flight MEADS vs Monte Carlo uncertainty estimates

5. UNCERTAINTY ASSESSMENT RESULTS

The uncertainty estimates from the three reconstruction methods were compared to assess their respective accuracies. Each method relied on a different set of inputs and their uncertainties reflect the accuracy of the inputs based on how the reconstructed state uncertainties were computed – either through propagation of covariance dynamics or transformation of input covariance. Ideally, there should exist some region of the uncertainty bounds of each reconstruction that overlap at each time point in the trajectory. In spite of differences in uncertainty between reconstruction methods, an overlapping region suggests that there is some value of the reconstructed state that all three methods agree upon. Such a result provides confidence in the reconstruction because the three semi-independent techniques are effectively offering support towards one another.

Figs. 2 and 3 show the uncertainty in angle of attack as estimated by the three methods of reconstruction. Fig. 2 shows the error between the inertial reconstruction and the aerodatabase and MEADS reconstructions. The 3-σ uncertainties are also shown in the figure to assess the relative performance of the reconstructions as compared to their uncertainties. Fig. 3 shows a comparison of the 3-σ uncertainties of each reconstruction. Similarly, angle of sideslip uncertainty is shown in Figs. 4-5.

The three angle of attack reconstructions agree with each other very well, with a maximum difference between any two reconstructions no greater than two degrees. The MEADS and inertial reconstructions agree best, with a maximum difference no greater than one degree. Uncertainties bounding angle of attack are greatest for the aerodatabase reconstruction with a 3-σ value of 2.35 degrees at 600 seconds. Over the trajectory, this uncertainty grows, reaching a maximum 3-σ value of 7.0 degrees at 748.2 seconds. The estimates of angle of attack uncertainty from the inertial and MEADS reconstructions are of roughly the same order, and are smaller than those of the aerodatabase reconstruction. For most of the reconstructed trajectory, the inertial estimates of 3-σ uncertainty are below one degree, with brief segments over one degree between 671.4 and 677.9 seconds, as well as after 741.6 seconds. The MEADS 3-σ uncertainty estimate exceeds one degree after 668.4 seconds and reaches a maximum value of 1.68 degrees at the end of the reconstruction.

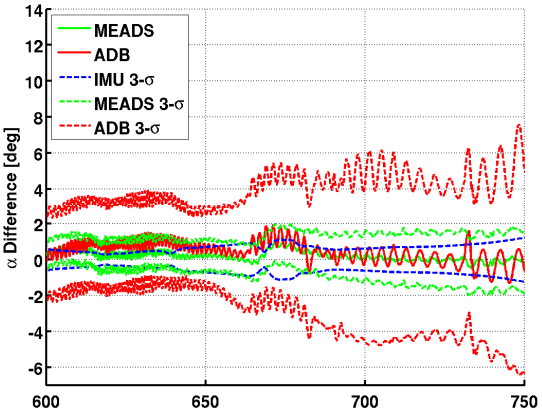

Fig 2. Angle of attack difference and uncertainty

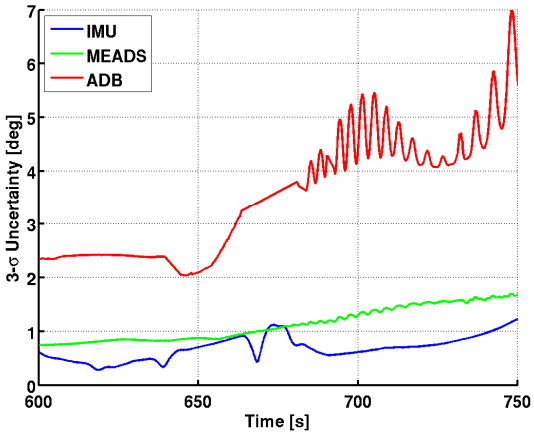

Fig 3. Angle of attack uncertainty

The three angle of sideslip reconstructions agree with each other very well, with a maximum difference between any two reconstructions no greater than 1.6 degrees. The differences between all three reconstructions are very similar, and the largest differences occur between the aerodatabase and MEADS reconstructions. As with the angle of attack reconstruction, the uncertainties bounding angle of sideslip are greatest for the aerodatabase reconstruction. The initial 3-σ uncertainty in the aerodatabase reconstruction is 2.7 degrees, and a minimum uncertainty of 2.3 degrees occurs at 650.2 seconds. The uncertainty grows after this minimum value and reaches a maximum of 4.0 degrees by the end of the reconstruction. The sideslip uncertainty estimate from the inertial reconstruction is significantly lower than that of the other two reconstruction methods. An initial value of 3-σ uncertainty is 0.29 degrees. The uncertainty grows, reaching a value of 2.73 degrees by the end of the reconstruction. The MEADS uncertainty estimate of angle of sideslip lies in between the uncertainty estimates of the inertial and aerodatabase reconstructions. The MEADS 3-σ uncertainty has an initial value of 1.25 degrees, over four times greater than the initial uncertainty in sideslip for the inertial estimate. While there is a large difference at the beginning of the reconstruction, the MEADS and inertial uncertainty estimates converge to roughly the same value of 3-σ uncertainty by the end of the reconstruction. The MEADS 3-σ estimate of sideslip uncertainty is 2.8 degrees at 770 seconds.

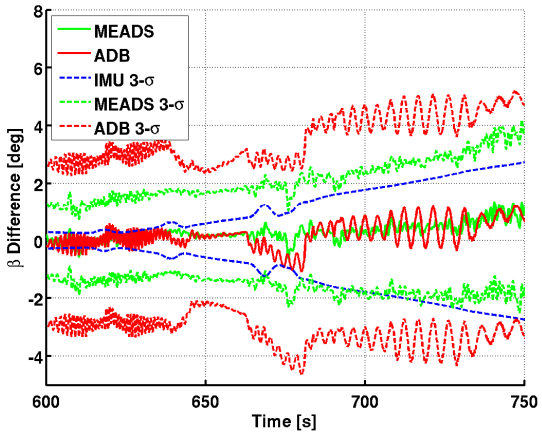

Fig 4. Angle of sideslip difference and uncertainty

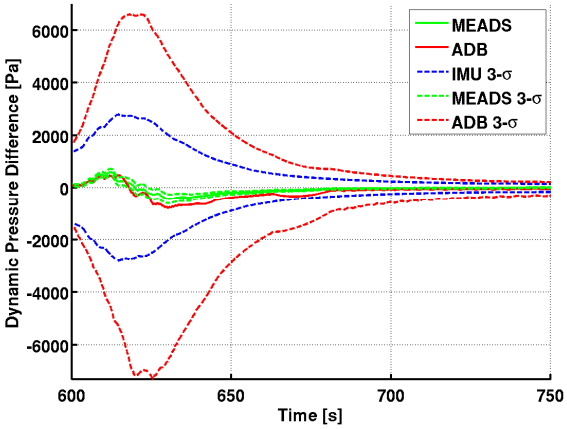

Fig 6. Dynamic pressure difference and uncertainty

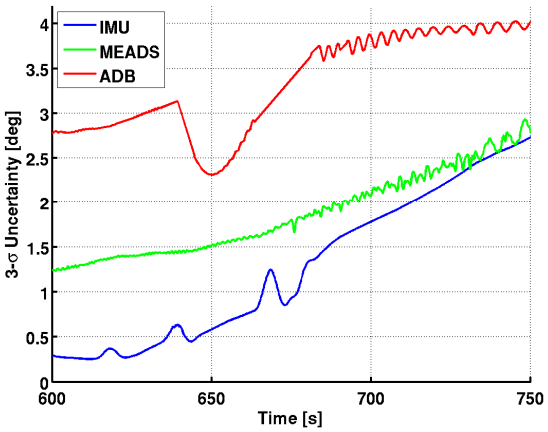

Fig 5. Angle of sideslip uncertainty

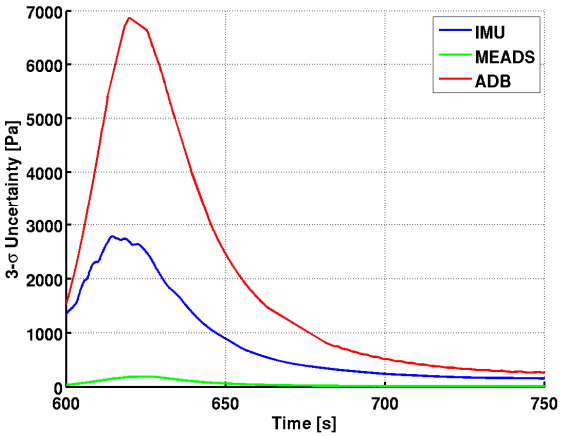

Fig 7. Dynamic pressure uncertainty

Figs. 6 and 7 show a comparison of the reconstructed dynamic pressure uncertainties from the three methods. The reconstructions are in reasonable agreement, with no two reconstructions differing by greater than 15%. The inertial and MEADS reconstructions are most similar with maximum differences of roughly four percent during the trajectory. The aerodatabase reconstruction deviates furthest from the other two methods, with maximum differences reaching 10.7% against the inertial reconstruction and 9.2% against the MEADS reconstruction.

The lowest uncertainties in dynamic pressure are seen in the MEADS reconstruction, with 1-σ uncertainties that do not exceed 0.75% of the reconstructed value, as shown in Fig. 9. This is in stark contrast with the inertial uncertainties, which vary between 5% and 12% of the reconstructed value, and the aerodatabase uncertainties, which vary between 14% and 15% of the reconstructed value. The 1-σ uncertainty estimates from the inertial and aerodatabase reconstructions relative to their reconstructed values are shown in Figs. 8 and 10. As expected, the MEADS pressure port data provides a higher accuracy reconstruction of parameters related to air data states.

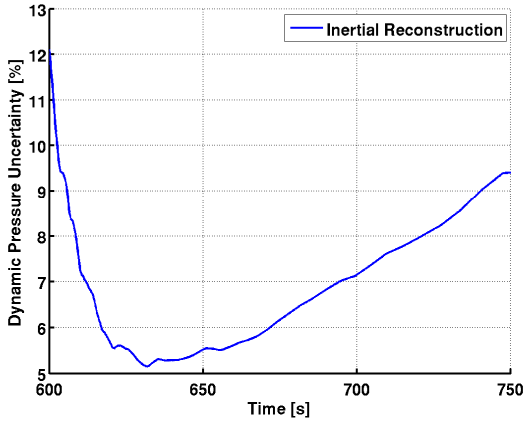

Fig 8. Dynamic pressure uncertainty - inertial reconstruction

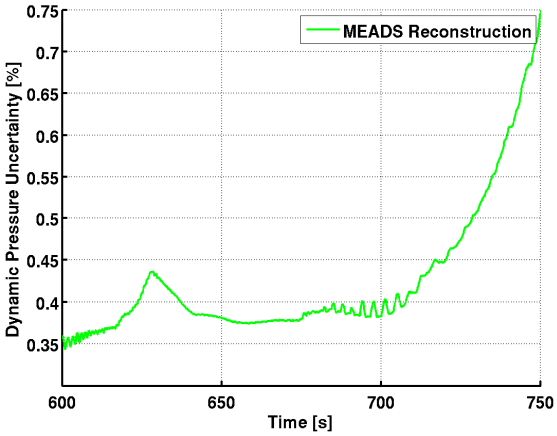

Fig 9. Dynamic pressure uncertainty - MEADS reconstruction

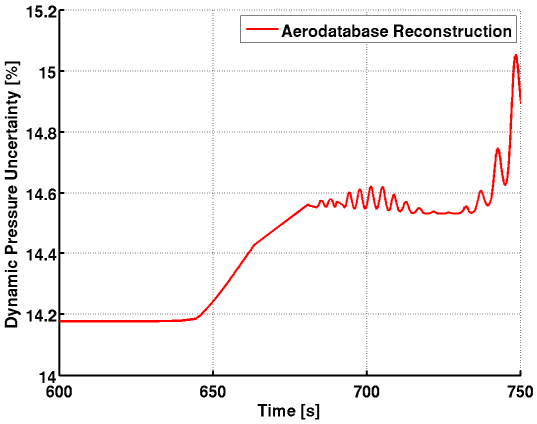

Figure 10. Dynamic pressure uncertainty - aerodatabase reconstruction

A comparison of the reconstructed density uncertainty estimates are shown in Figs. 11 and 12. Whereas the inertial reconstruction relies on a pre-determined atmosphere model, the MEADS and aerodatabase reconstructions of density are able to estimate density directly from flight data. Between 620 and 680 seconds, the hypersonic region of flight, the inertial reconstruction agrees best with the MEADS reconstruction of density, with differences no greater than (roughly) 3%. Beyond 700 seconds, during supersonic flight, the inertial reconstruction agrees best with the aerodatabase estimate of density, with differences approximately on the order of 2% to 4%. The difference between the MEADS and aerodatabase reconstructions grows steadily from the beginning of the reconstruction reaching a maximum difference of 10.3%.

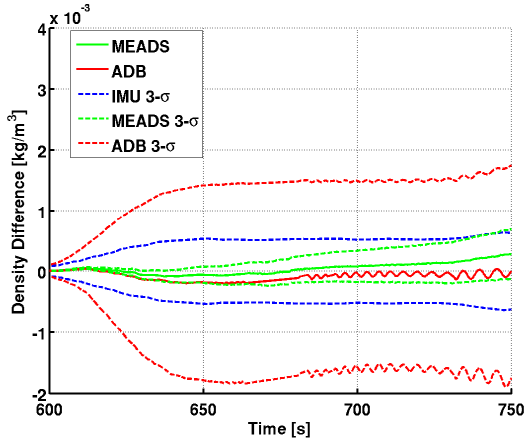

Figure 11. Density difference and uncertainty

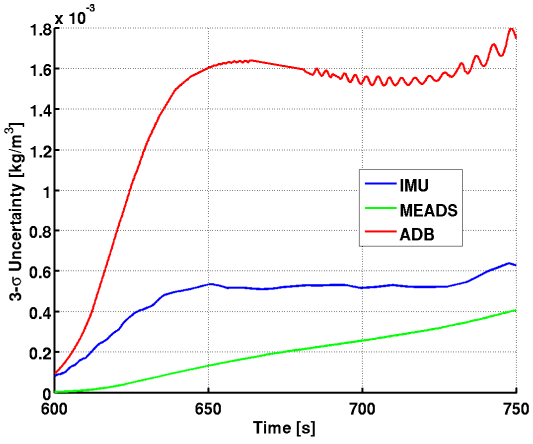

Figure 12. Density uncertainty

A comparison of the 3-σ density uncertainty estimates are shown in Fig. 12. Similar to the dynamic pressure uncertainty estimates, the density uncertainties are lowest for the MEADS reconstruction algorithm. The 1-σ density uncertainties as a percentage of the reconstructed value are shown in Figs. 13-15. The MEADS uncertainties do not exceed 5% of their reconstructed values over the reconstructed trajectory. This is significantly larger than the MEADS dynamic pressure uncertainties, most likely due to the very low

uncertainty contributions of velocity in computing dynamic pressure. The aerodatabase and inertial uncertainty estimates of density are very similar to their dynamic pressure uncertainty estimates. These results provide a high level of confidence in the reconstructions because the uncertainties are small and the three reconstructions agree reasonably well.

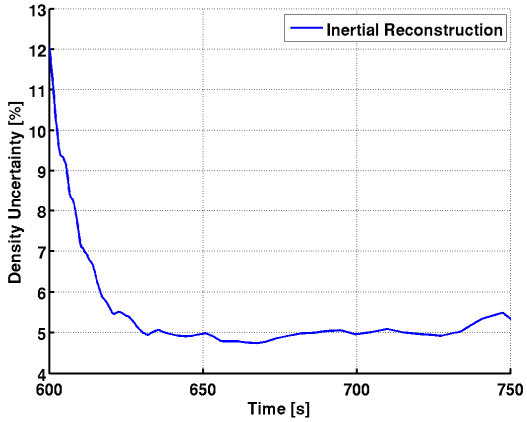

Figure 13. Density uncertainty - inertial reconstruction

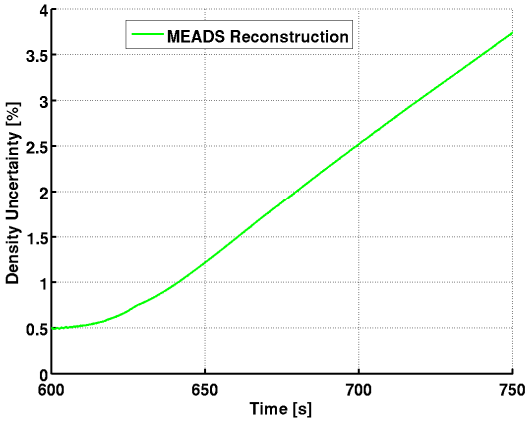

Figure 2. Density uncertainty - MEADS reconstruction

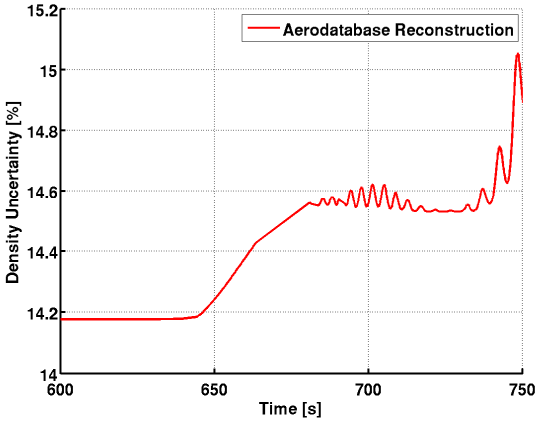

Figure 3. Density uncertainty - aerodatabase reconstruction

6. CONCLUSION

Three semi-independent methods were applied to perform reconstruction of the MSL EDL trajectory. Each method utilized a different set of inputs to reconstruct several common parameters. Additionally, the reconstructions provided assessments of the accuracy of each reconstruction through analysis of the state's statistical properties. A novel method of uncertainty estimation was used by the aerodatabase reconstruction algorithm. This technique performed a transformation of input covariances into output covariances through linearization of the estimation equations. Each method of reconstruction and uncertainty estimation was described and the resulting uncertainty estimates of reconstructed states were compared. The results between the three approaches showed strong agreement, and overlapping uncertainty bounds, indicating accurate and consistent reconstruction by all three methods.

7. REFERENCES

1. Euler, E. A., Adams, G. L., and Hopper, F. W., "Design and Reconstruction of the Viking Lander Descent Trajectories," *Journal of Guidance and Control*, Vol. 1, No. 5, 1978, pp. 372–378.

2. Spencer, D. A., Blanchard, R. C., Braun, R. D., Kallameyn, P. H., and Thurman, S. W., "Mars Pathfinder Entry, Descent, and Landing Reconstruction," *Journal of Spacecraft and Rockets*, Vol. 36, No. 3, 1999, pp. 357–366.

3. Withers, P., Towner, M. C., Hathi, B., and Zarnecki, J. C., "Analysis of Entry Accelerometer Data: A Case Study of Mars Pathfinder," *Planetary and Space Science*, Vol. 51, 2003, pp. 541–561.

4. Withers, P. and Smith, M. D., "Atmospheric Entry Profiles from the Mars Exploration Rovers Spirit and Opportunity," *Icarus*, Vol. 185, 2006, pp. 133-142.

5. Blanchard, R. C., "Entry Descent and Landing Trajectory and Atmosphere Reconstruction for the Mars Exploration Rovers Missions A and B," George Washington University, Final Report, NASA-JPL Subcontract CCNS20568F, April 2008.

6. Blanchard, R. C. and Desai, P. N., "Mars Phoenix Entry, Descent, and Landing Trajectory and Atmosphere Reconstruction," *Journal of Spacecraft and Rockets*, Vol. 48, No. 5, 2011, pp. 809–821.

7. Karlgaard, C. D., Tartabini, P. V., Blanchard, R. C., Kirsch, M., and Toniolo, M. D., "Hyper–X Post–Flight Trajectory Reconstruction," *Journal of Spacecraft and Rockets*, Vol. 43, No. 1, 2006, pp. 105–115.

8. Nørgaard, M., Poulsen, N. K., and Ravn, O., "New Developments in State Estimation for Nonlinear Systems," *Automatica*, Vol. 36, No. 11, 2000, pp. 1627-1638.

9. Schoenenberger, M., Dyakonov, A., Buning, P., Scallion, W., and Van Norman, J., "Aerodynamic Challenges for the Mars Science Laboratory Entry, Descent and Landing," AIAA Paper 2009-3914, June 2009.

10. Dyakonov, A., Schoenenberger, M., and Van Norman, J., "Hypersonic and Supersonic Static Aerodynamics of Mars Science Laboratory Entry Vehicle," AIAA Paper 2012-2999, June 2012.

11. Karlgaard, C., Kutty, P., Schoenenberger, M., Shidner, J., and Munk, M., "Mars Entry Atmospheric Data System Trajectory Reconstruction Algorithms and Flight Results,'' AIAA Paper 2013-0028, 51st AIAA Aerospace Sciences Meeting, Grapevine, TX, January 2013.

12. Karlgaard, C., Beck, R., O'Keefe, S., Siemers, P., White, B., Engelund, W., and Munk, M., "Mars Entry Atmospheric Data System Modeling and Algorithm Development," AIAA Paper 2009-3916, 41st AIAA Thermophysics Conference, San Antonio, TX, June 2009.

13. Pruett, C., Wolf, H., Heck, M., and Siemers, P., "Innovative Air Data System for the Space Shuttle Orbiter," *Journal of Spacecraft and Rockets*, Vol. 20, No. 1, 1983, pp. 61-69.

14. Lugo, R., Tolson, R., and Schoenenberger, M., "Trajectory Reconstruction and Uncertainty Analysis using Mars Science Laboratory Pre-Flight Scale Model Aeroballistic Testing," AIAA Paper 2013-1132, 51st AIAA Aerospace Sciences Meeting, Grapevine, TX, January 2013.

15. Little, A., Bose, D., Karlgaard, C., Munk, M., Kuhl, C., Schoenenberger, M., Antill, C., Verhappen, R., Kutty, P., and White, T., "The Mars Science Laboratory (MSL) Entry, Descent and Landing Instrumentation (MEDLI): Hardware Performance and Data Reconstruction," AAS Paper 13-078, AAS Guidance and Control Conference, Breckenridge, CO, February 2013.

16. Munk, M., Little, A., Kuhl, C., Bose, D., and Santos, J., "The Mars Science Laboratory (MSL) Entry, Descent, and Landing Instrumentation (MEDLI) Hardware," AAS Paper 13-310, AAS/AIAA Space Flight Mechanics Meeting, Lihue, HI, February 2013.